

SCIENTIFIC REPORTS

OPEN

Effect of Different Gate Lengths on Polarization Coulomb Field Scattering Potential in AlGaN/GaN Heterostructure Field-Effect Transistors

Peng Cui¹, Jianghui Mo², Chen Fu¹, Yuanjie Lv², Huan Liu³, Aijie Cheng³, Chongbiao Luan⁴, Yang Zhou⁵, Gang Dai⁵ & Zhaojun Lin¹

The AlGaN/GaN heterostructure field-effect transistors with different gate lengths were fabricated. Based on the chosen of the Hamiltonian of the system and the additional polarization charges, two methods to calculate PCF scattering by the scattering theory were presented. By comparing the measured and calculated source-drain resistances, the effect of the different gate lengths on the PCF scattering potential was confirmed.

AlGaN/GaN heterostructure field-effect transistors (HFETs) have emerged as excellent devices for high-frequency and high-power applications^{1–14}, owing to their superior properties such as high electron mobility, high saturation electron velocity, and large critical breakdown field^{15–25}. Polarization Coulomb field (PCF) scattering, stemming from the non-uniform distribution of the strain in the AlGaN barrier layer, can affect the electron mobility, parasitic source access resistance, transconductance, and device linearity in AlGaN/GaN HFETs^{26–40}. Based on the perturbation theory, the theoretical model of PCF scattering has been established³¹, which makes it possible to quantitative study of PCF scattering^{35–40}. The Hamiltonian of electrons in the source-drain channel can be split into two parts $\hat{H} = \hat{H}_0 + \hat{H}'$, where \hat{H}_0 is known as the Hamiltonian of the unperturbed system, and \hat{H}' is called the perturbation. For PCF scattering, \hat{H}' originates from the effect of additional polarization charges on the channel electrons, and is referred as the PCF scattering potential. The polarization charges underneath the gate region can be altered by the gate bias⁴¹, leading to the polarization charges at the AlGaN/GaN interface uneven. The non-uniform distribution of polarization charges can generate the PCF scattering potential. The gate length is relevant with the non-uniform distribution of polarization charges^{26,30,35,38}. Hence, the different gate lengths can affect the PCF scattering potential. If the PCF scattering potential is large enough, the accuracy of the PCF scattering model based on the perturbation theory may be challenged. Therefore, exploring the effect of different gate lengths on PCF scattering potential is necessary.

In this paper, the AlGaN/GaN HFETs with different gate lengths were fabricated. By comparing the measured and calculated source-drain resistances, the influence of different gate lengths on PCF scattering potential was explored.

Results and Discussion

As shown in Fig. 1, the AlGaN/GaN HFETs with source-drain spacing (L_{SD}) of 20 μm and the gate width (W_G) of 100 μm were fabricated. The Schottky gate was symmetrically placed in the middle between the source and drain ohmic contacts. The gate lengths (L_G) of Sample 1, 2, and 3 are 4, 10, and 16 μm , respectively. The DC I - V characteristics for the three samples were measured, as shown in Fig. 2(a). From the I - V characteristics, the total

¹School of Microelectronics, Shandong University, Jinan, 250100, China. ²National Key Laboratory of Application Specific Integrated Circuit (ASIC), Hebei Semiconductor Research Institute, Shijiazhuang, 050051, China. ³School of Mathematics, Shandong University, Jinan, 250100, China. ⁴Key Laboratory of Pulsed Power, Institute of Fluid Physics, CAEP, Mianyang, 621999, China. ⁵Microsystem and Terahertz Research Center, China Academy of Engineering Physics, Chengdu, 610200, China. Correspondence and requests for materials should be addressed to Z.L. (email: linzj@sdu.edu.cn)

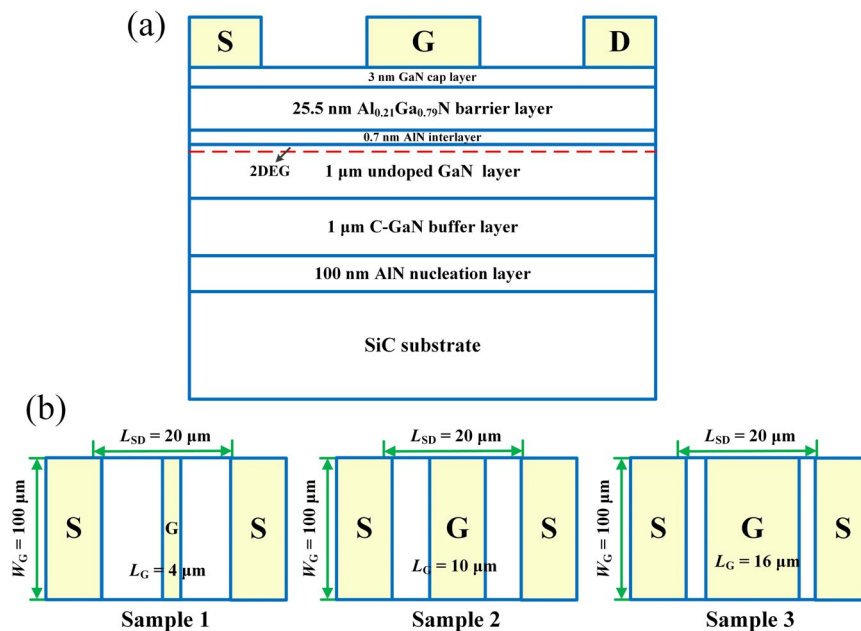


Figure 1. (a) Cross-sectional view of the AlGaN/GaN HFETs. (b) Top view of the three samples.

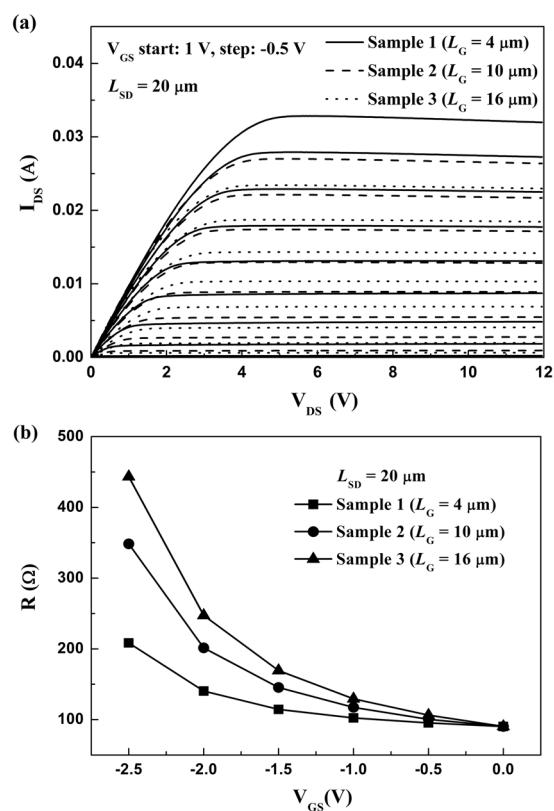


Figure 2. (a) The measured DC I - V characteristics and (b) the measured total resistance R in the source-drain channel as a function of gate bias for the three samples.

resistance R in the source-drain channel as a function of gate bias can be obtained by $R = V_{DS}/I_{DS} - 2R_C$, as shown in Fig. 2(b). Here I_{DS} refers to the source-drain current corresponding to the source-drain voltage $V_{DS} = 0.1$ V. The C - V characteristics for the three samples were performed, as shown in Fig. 3(a). Integration of measured gate

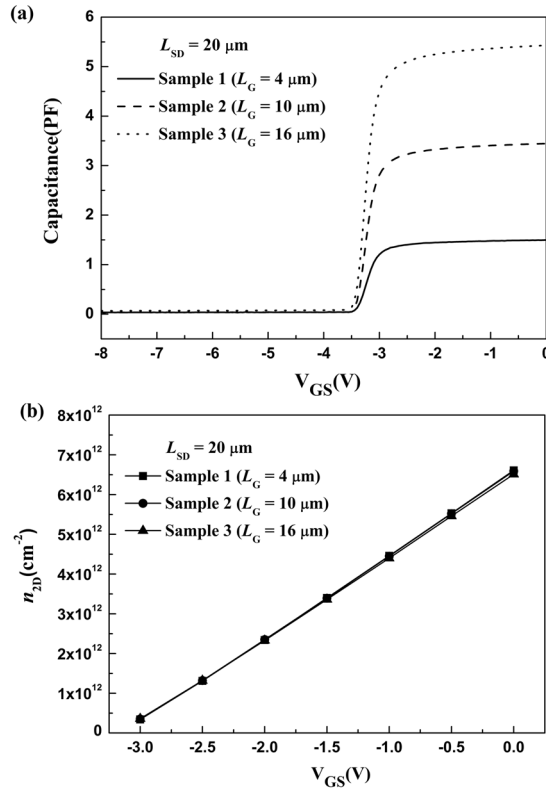


Figure 3. (a) The measured C-V characteristics and (b) the two-dimensional electron gas (2DEG) electron density n_{2D} under the gate region as a function of gate bias for the three samples.

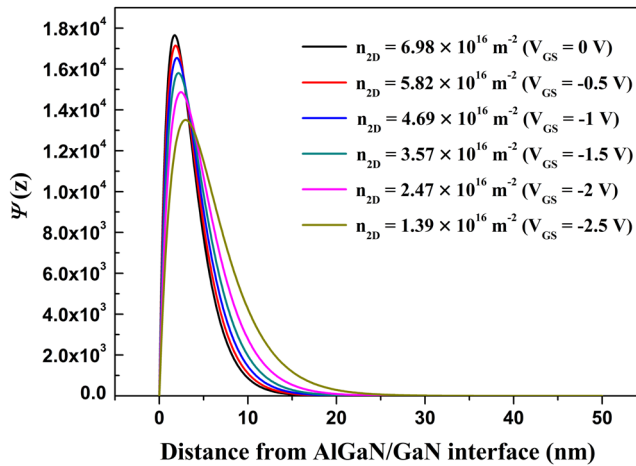


Figure 4. The obtained $\psi(z)$ as a function of the distance from AlGaIn/GaN interface under different n_{2D} (here n_{2D} corresponds to the electron density under the gate region as a function of gate bias).

capacitance over gate bias yielded the two-dimensional electron gas (2DEG) electron density n_{2D} under the gate region^{26–28,31}, as shown in Fig. 3(b).

In AlGaIn/GaN HFETs, the main scattering mechanisms include polarization Coulomb field (PCF), polar optical phonon (POP), acoustic phonon (AP), interface roughness (IFR), and dislocation (DIS) scatterings^{26,31,42–50}. R can be determined by the scattering theories of the 2DEG electrons in AlGaIn/GaN HFETs^{31,38,46–50}.

In AlGaIn/GaN HFETs, the 2DEG electrons can be written as $\Psi(x, y, z) = A^{-1/2}\psi(z)\exp(ik_x x + ik_y y)$ ^{31,38,46,48,50}. Here A is the normalization constant, k_x, k_y refer to the components of k in the x -direction and y -direction, respectively. $\psi(z) = (b^3 z^2/2)^{1/2}\exp(-bz/2)$ refers to the quantized wave in z -direction and $b = (33m^*e^2 n_{2D}/8\epsilon_0\epsilon_s\hbar^2)^{1/3}$ is the variational parameter. m^* refers to the electron effective mass of GaN, ϵ_0 is the dielectric permittivity, and ϵ_s refers to the static dielectric constant of GaN. The $\psi(z)$ under different n_{2D} can be calculated, as shown in Fig. 4. It is apparent $\psi(z)$ is closely relevant with n_{2D} . The larger n_{2D} is, the closer the 2DEG electrons to the AlGaIn/GaN

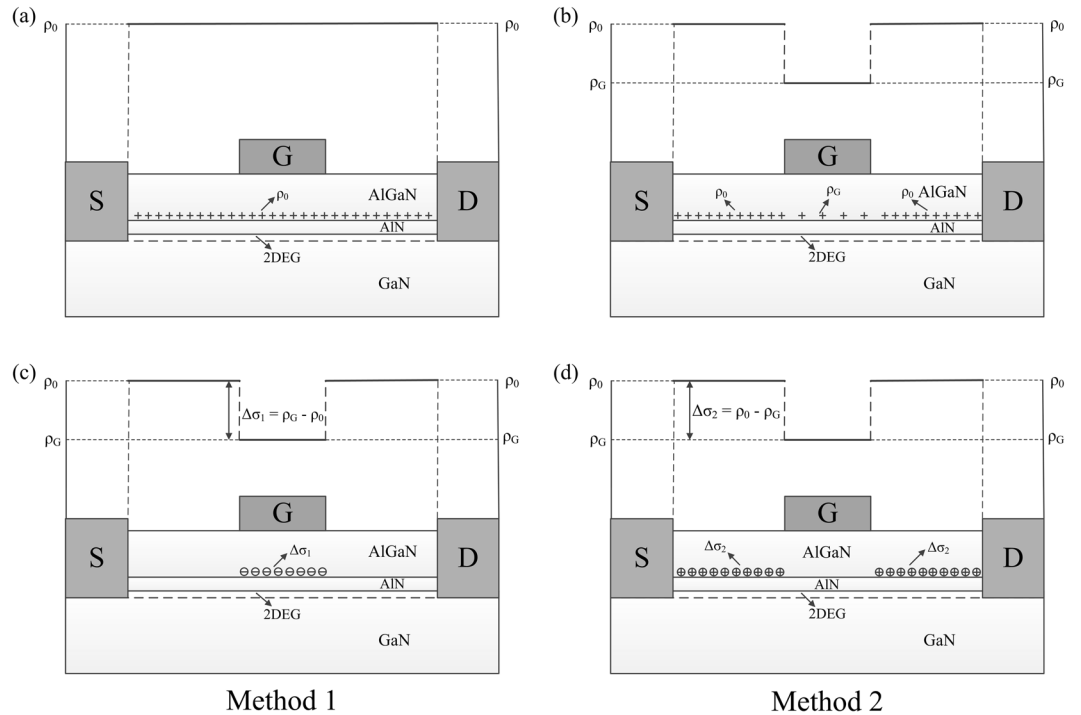


Figure 5. The schematic of the polarization charge distribution at the AlGaIn/GaN interface (a) without gate bias (b) with the negative gate bias; The schematic of the additional polarization charge distribution at the AlGaIn/GaN interface (c) for Method 1 and (d) for Method 2.

interface is. Hence, $\Psi(x, y, z)$ depends on n_{2D} . We note that n_{2D} under the gate region is increased with the gate bias, while n_{2D} under the free-contact region (including the gate-source region and the gate-drain region) is constant. Therefore, it is different for $\Psi(x, y, z)$ under the gate region and the free-contact region.

PCF scattering originates from the non-uniform distributed polarization charges at the AlGaIn/GaN interface^{26,27,31}. Before device processing, because of the spontaneous and piezoelectric polarization, there are uniform distributed polarization charges at the AlGaIn/GaN interface, as shown in Fig. 5(a), which cannot scatter the channel electrons. The charge density of the uniform distributed polarization charges is named as ρ_0 . Due to the converse piezoelectric effect, the strain of the AlGaIn barrier layer underneath the gate region can be altered by the gate bias, as shown in Fig. 5(b). The polarization charge density under the gate region, labeled as ρ_G , can be calculated as following^{36–38,41}

$$\rho_G = \frac{e_{33}^2}{C_{33}} \cdot \frac{V_{GS}}{d_{AlGaIn}} + \rho_0, \tag{1}$$

where e_{33} and C_{33} are the piezoelectric coefficient and the elastic stiffness tensor of AlGaIn, respectively, V_{GS} is the gate-source voltage and d_{AlGaIn} is the thickness of the AlGaIn barrier layer. The free-contact region cannot be affected by the gate bias, where the polarization charges is still equal to ρ_0 . The non-uniform distributed polarization charges between the gate region and the free-contact region can induce PCF scattering potential. The difference between the non-uniform distributed polarization charges and the uniform distributed polarization charges is defined as the additional polarization charges, labeled as $\Delta\sigma$. The PCF scattering potential originates from $\Delta\sigma$, and the determination of $\Delta\sigma$ is based on the chosen of the Hamiltonian of electrons.

The perturbation theory is used in the PCF scattering calculation. The Hamiltonian of electrons in the source-drain channel can be split into two parts $\hat{H} = \hat{H}_0 + \hat{H}'$, where \hat{H}_0 is known as the Hamiltonian of the unperturbed system, and \hat{H}' is very small compared to \hat{H}_0 . As a result, \hat{H}' is called the perturbation, for its effects on the energy spectrum and eigenfunctions will be small. Here \hat{H}' originates from the effect of additional polarization charges on the channel electrons, and is referred as the PCF scattering potential. When the gate bias is applied to the AlGaIn barrier layer, the electrons under the gate region can be modulated. Then in the source-drain channel electron system, there are two types of \hat{H}_0 , which are the \hat{H}_0 for the electrons under the gate region, and the \hat{H}_0 for the electrons under the free contact region. Both can likely be treated as \hat{H}_0 .

If the \hat{H}_0 for the electrons under the free-contact region is chosen, as shown in Fig. 5(c), $\Psi(x, y, z)$ in the free-contact region is used. This is defined as the Method 1. Because the 2DEG electron density under the free-contact region is equal to n_{2D0} (here n_{2D0} refers to the 2DEG electron density under the gate region corresponding to $V_{GS} = 0V$), $n_{2D} = n_{2D0}$ is used in $\Psi(x, y, z)$. The polarization charges under the free-contact region is ρ_0 , therefore the additional charges can be obtained by^{36–38,41}

$$\Delta\sigma_1 = \rho_G - \rho_0 = \frac{e_{33}^2}{C_{33}} \cdot \frac{V_{GS}}{d_{\text{AlGaN}}}. \quad (2)$$

The additional polarization charges $\Delta\sigma_1$ is under the gate region. Based on the obtained $\Delta\sigma_1$, the PCF scattering potential can be written as^{31,37,38,50}

$$V_1(x, y, z) = -\frac{e}{4\pi\epsilon_s\epsilon_0} \int_{-\frac{L_G}{2}}^{\frac{L_G}{2}} dx' \int_0^{W_G} \frac{\Delta\sigma_1}{\sqrt{(x-x')^2 + (y-y')^2 + z^2}} dy'. \quad (3)$$

If the \hat{H}_0 for the electrons under the gate region is chosen, as shown in Fig. 5(d), $\Psi(x, y, z)$ under the gate region is used. This is defined as the Method 2. Here n_{2D} under the gate region is used for $\Psi(x, y, z)$. The additional polarization charges can be determined by

$$\Delta\sigma_2 = \rho_0 - \rho_G = -\frac{e_{33}^2}{C_{33}} \cdot \frac{V_{GS}}{d_{\text{AlGaN}}}. \quad (4)$$

The additional polarization charges $\Delta\sigma_2$ is under the gate-source region and the gate-drain region. Based on the obtained $\Delta\sigma_2$, the PCF scattering potential can be expressed by^{31,37,38,50}

$$V_2(x, y, z) = -\frac{e}{4\pi\epsilon_s\epsilon_0} \int_{-L_{GS}-\frac{L_G}{2}}^{-\frac{L_G}{2}} dx' \int_0^{W_G} \frac{\Delta\sigma_2}{\sqrt{(x-x')^2 + (y-y')^2 + z^2}} dy' \\ - \frac{e}{4\pi\epsilon_s\epsilon_0} \int_{\frac{L_G}{2}}^{L_{GD}+\frac{L_G}{2}} dx' \int_0^{W_G} \frac{\Delta\sigma_2}{\sqrt{(x-x')^2 + (y-y')^2 + z^2}} dy'. \quad (5)$$

Here L_{GS} and L_{GD} refer to the gate-source spacing and gate-drain spacing, respectively.

In the next calculation processing, as discussed above, the different wave functions $\Psi(x, y, z)$ and the PCF scattering potential $V(x, y, z)$ are adopted for two different methods. With the obtained $\Psi(x, y, z)$ and $V(x, y, z)$, the scattering matrix element is given by^{31,37,38,50}

$$M_{k \rightarrow k'} = A^{-1} \int_0^\infty \psi_k^*(z) \left[\int_{-\frac{L_{SD}}{2}}^{\frac{L_{SD}}{2}} dx \int_0^{W_G} V(x, y, z) \right. \\ \left. \times \exp(-iq_x x - iq_y y) dy \right] \psi_k(z) dz \\ = A^{-1} \int_0^\infty \psi_k^*(z) [V(q_x, q_y, z)] \psi_k(z) dz. \quad (6)$$

where q_x, q_y refer to the components of the wave vector \mathbf{q} in the x -direction and y -direction, respectively. The change in \mathbf{q} during a scattering process is related to the scattering angle θ between initial state \mathbf{k} and final state \mathbf{k}' by $q = [2(2m^*\hbar^{-2}E)^{1/2} \sin(\theta/2)]$.

Then the energy dependent scattering rate for the PCF scattering can be obtained^{31,37,38,50}

$$\frac{1}{\tau_{\text{PCF}}(E)} = \frac{Am^*}{2\pi\hbar^3} \int_{-\pi}^{\pi} \left| \frac{M_{k \rightarrow k'}}{S(q, T_e)} \right|^2 (1 - \cos\theta) d\theta. \quad (7)$$

where \hbar is the Planck constant. The screening function $S(q, T_e)$ is^{31,37,38,50}

$$S(q, T_e) = 1 + \frac{e^2 F(q) \Pi(q, T_e, E)}{2\epsilon_0\epsilon_s q}. \quad (8)$$

Here the form factor $F(q)$ is^{31,37,38,50}

$$F(q) = \int_0^\infty \int_0^\infty \psi^2(z) \psi^2(z') \exp(-q|z - z'|) dz dz'. \quad (9)$$

The closer the 2DEG electrons to the additional polarization charges is, the stronger the Coulomb screening effect is. Therefore, the 2DEG channel electrons, which are the nearest to the additional polarization charges, are chosen in Eq. (9). That is, for Method 1, $\Delta\sigma_1$ is under the gate region and the electron wave function under the gate region is used in Eq. (9). Conversely, for Method 2, $\Delta\sigma_2$ is under the free-contact region and the electron wave function under the free-contact region is used in Eq. (9).

The polarizability function $\Pi(q, T_e, E)$ is^{31,37,38,50}

$$\Pi(q, T_e, E) = \frac{m^*}{4\pi\hbar^2 k_B T_e} \int_0^\infty \frac{1 - \Theta(q - 2k_F)[1 - (2k_F/q)^2]^{1/2}}{\cosh^2[(E_F - E)/2k_B T_e]} dE. \quad (10)$$

In this equation, $\Theta(x)$ is the usual step function, $k_F = (2\pi n_{2D})^{1/2}$ is the Fermi wave vector, T_e is the electron temperature, E_F is the Fermi energy, and E is the energy.

At the end, the momentum relaxation time τ_{PCF} for PCF scattering can be got^{31,37,38,50}

$$\tau_{PCF} = \int \tau_{PCF}(E) E \frac{\partial f_0(E)}{\partial E} dE / \int E \frac{\partial f_0(E)}{\partial E} dE. \quad (11)$$

where f_0 , the Fermi function, is

$$f_0(E) = \frac{1}{\exp[(E - E_F)/k_B T_e] + 1}. \quad (12)$$

Here k_B is the Boltzmann constant.

The momentum relaxation times τ_{POP} , τ_{AP} , τ_{IFR} , and τ_{DIS} for POP, AP, IFR, and DIS scatterings were obtained by the pre-existing calculation formulas^{31,37,38,50}. Considering n_{2D} between the gate region and the free-contact region is different, the R for three samples can be determined with the resistance R_G under the gate region plus the resistance R_F under the free-contact region^{31,37,38,50}.

$$R = R_G + R_F = \frac{m^* L_G}{n_{2D} e^2 W_G} \left(\frac{1}{\tau_{PCF}} + \frac{1}{\tau_{POP}^G} + \frac{1}{\tau_{AP}^G} + \frac{1}{\tau_{IFR}^G} + \frac{1}{\tau_{DIS}^G} \right) + \frac{m^* (L_{GS} + L_{GD})}{n_{2D0} e^2 W_G} \left(\frac{1}{\tau_{PCF}^F} + \frac{1}{\tau_{POP}^F} + \frac{1}{\tau_{AP}^F} + \frac{1}{\tau_{IFR}^F} + \frac{1}{\tau_{DIS}^F} \right). \quad (13)$$

Here τ_{POP}^G , τ_{AP}^G , τ_{IFR}^G , and τ_{DIS}^G refer to the momentum relaxation times for POP, AP, IFR, and DIS scatterings under the gate region, respectively. τ_{POP}^F , τ_{AP}^F , τ_{IFR}^F , and τ_{DIS}^F refer to the momentum relaxation times for POP, AP, IFR, and DIS scatterings under the free-contact region, respectively. The calculated R for the three samples was shown in Fig. 6. Firstly, there is a distinct difference between the measured R and the calculated R excluding PCF scattering. This means PCF scattering is not ignorable in AlGaIn/GaN HFETs. Then R , including the calculated PCF scattering by the two methods, was obtained. It is apparent that the calculated results by Method 1 has better accord with the measured values for Sample 1, and the calculated results by Method 2 agree well with the measured values for Sample 3. Different from the two samples, the calculated results by both Method 1 and Method 2 have a significant difference with the measured values for Sample 2. This phenomenon can be explained as following.

POP, AP, IFR, and DIS scatterings are consistent for the three samples, therefore the difference should come from the PCF scattering calculation with the two methods. PCF scattering is calculated by the scattering model based on the perturbation theory. The perturbation theory is most suitable when \hat{H} is very close to \hat{H}_0 and PCF scattering can be solved exactly. To this end, H' should be far less than H_0 . The less H' is, the more precise the calculated PCF scattering is. H' is the PCF scattering potential $V(x, y, z)$. Therefore, for a more clear presentation, the average value of $V(x, y, z)$ can be expressed by^{36–38}

$$\bar{V} = \frac{1}{L_{SD} \cdot W_G \cdot z} \int_{-\frac{L_{SD}}{2}}^{\frac{L_{SD}}{2}} dx' \int_0^{W_G} dy \int_0^z V(x, y, z) dz. \quad (14)$$

Here, considering the 2DEG wave function distribution in z -direction, as shown in Fig. 4, $z = 50$ nm is adopted. The calculated \bar{V} with two methods for the three samples was shown in Fig. 7.

For sample 1, because $L_G = 4 \mu\text{m}$ and $L_{SD} = 20 \mu\text{m}$, the free-contact region is larger than the gate region. With Method 2, $\Delta\sigma_2$ and $V_2(x, y, z)$ are used. Because of the large free-contact region, there are numerous additional polarization charges under the free-contact region, which will induce a large PCF scattering potential, namely a larger H' . The large H' can affect the precision of the calculated PCF scattering. Conversely, with Method 1, $\Delta\sigma_1$ and $V_1(x, y, z)$ are adopted. Due to the small gate length, the additional polarization charges underneath the gate region is small for a large source-drain distance, leading to smaller $V(x, y, z)$ or H' . As shown in Fig. 7(a), the \bar{V} obtained by Method 1 is smaller than that obtained by Method 2. The smaller \bar{V} means a less H' , which can improve the precision of the PCF scattering calculation. This means for a small gate length, it is appropriate that $V_1(x, y, z)$ is treated as the PCF scattering potential.

For Sample 3, because $L_G = 16 \mu\text{m}$ and $L_{SD} = 20 \mu\text{m}$, the gate region is larger than the free-contact region. As discussed above, in order to obtain a small H' , the additional polarization charges under the free-contact region should be chosen. This means $\Delta\sigma_2$ and $V_2(x, y, z)$ should be adopted. As shown in Fig. 7(c), the \bar{V} obtained by Method 2 is smaller than that obtained by Method 1. Hence Method 2 is more suitable for the PCF scattering calculation, which agrees well with the results as shown in Fig. 6(c). This indicates that for a large gate length, $V_2(x, y, z)$ should be adopted as the PCF scattering potential.

For Sample 2, on account of $L_G = 10 \mu\text{m}$ and $L_{SD} = 20 \mu\text{m}$, the gate region is equal to the free-contact region. H' obtained by the two methods both cannot be small enough, as shown in Fig. 7(b), which affect the precision of the PCF scattering calculation. Therefore, the obtained R by two methods has a significant difference with the measured values.

In addition, as the gate bias is more negative, the number of additional polarization charges ($\Delta\sigma_1$ and $\Delta\sigma_2$) is increased. The increased $\Delta\sigma$ can increase the $V(x, y, z)$ and H' , as show in Fig. 7, which also can reduce the precision of the PCF scattering calculation. That is why as the gate bias is decreased, the deviation between the calculated R and the measured R is increased. This further indicated that the explanation for the effect of different gate lengths on PCF scattering potential is suitable.

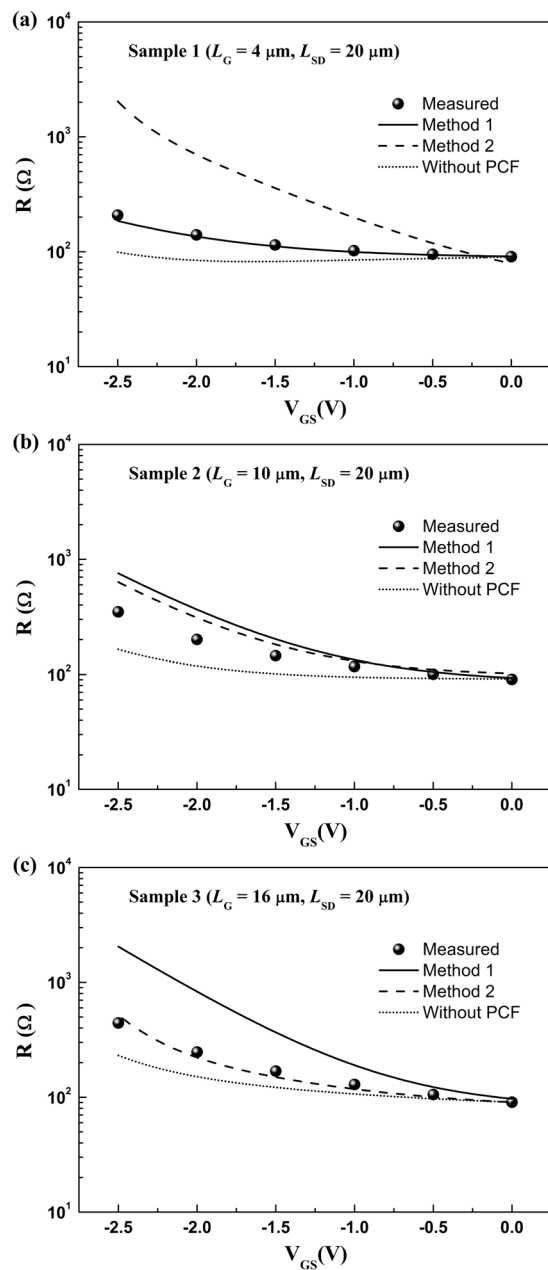


Figure 6. The measured source-drain channel resistance (Measured), and the calculated source-drain channel resistance calculated by Method 1 (Method 1), Method 2 (Method 2) as well as without PCF scattering (Without PCF), as a function of gate bias for (a) Sample 1, (b) Sample 2, and (c) Sample 3, respectively.

Conclusions

In summary, with the measured and calculated source-drain channel resistances for the AlGaIn/GaN HFETs with different gate lengths, the effect of different gate lengths on PCF scattering potential was analyzed. It is found that the gate length can influence the determination of the Hamiltonian of the system and the additional polarization charges, and then affect the PCF scattering potential. This study offers an effective way for improving the precision of the PCF scattering model.

Methods

Sample fabrication. The AlGaIn/GaN heterostructure was grown by molecular beam epitaxy (MBE) on a sapphire substrate. The epitaxial structure consists of, from the bottom to the top, a 100-nm-thick AlN nucleation layer, a 1- μm -thick GaN buffer layer with carbon doped, a 1- μm -thick GaN channel layer, a 0.7-nm-thick AlN interlayer, a 25.5-nm-thick AlGaIn barrier layer with 21% Al composition, and a 3-nm-thick GaN cap layer. A high sheet electron density (n_{2D}) of $8.4 \times 10^{12} \text{ cm}^{-2}$ and a high electron mobility (μ) of $2340 \text{ cm}^2/\text{V}\cdot\text{s}$ were obtained by Hall measurement. Device isolation was achieved by inductively coupled plasma reactive ion etching

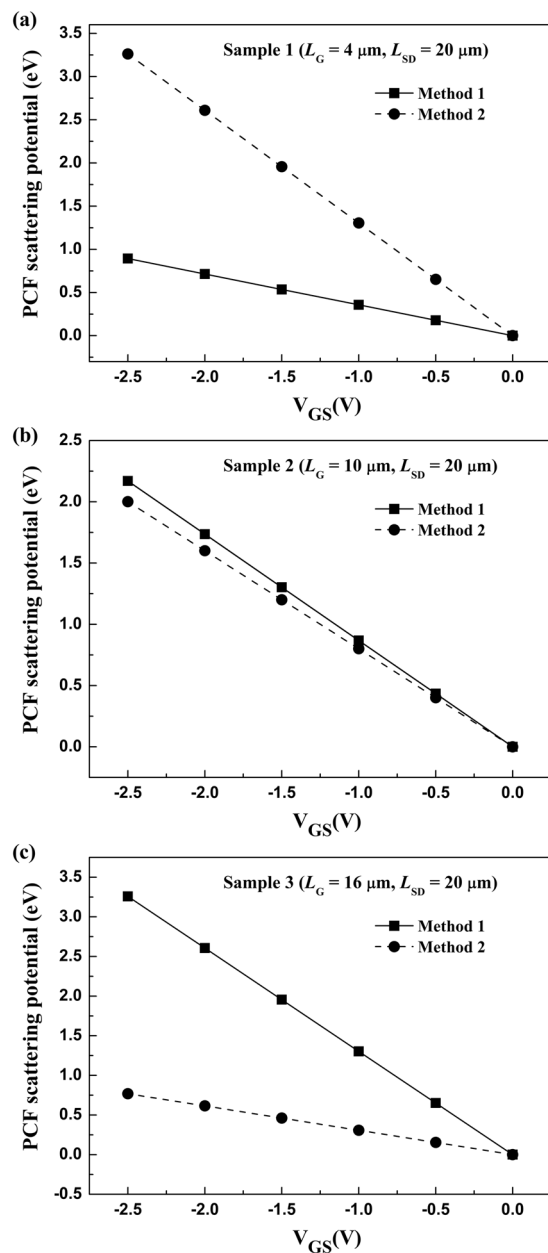


Figure 7. The obtained average value of $V(x, y, z)$ by two methods as a function of gate bias for (a) Sample 1, (b) Sample 2, and (c) Sample 3, respectively.

(ICP-RIE) using BCl_3/Cl_2 gas mixture. Ti/Al/Ni/Au-based ohmic metal stack was then deposited and annealed in N_2 ambient at 850°C for 30 s. The ohmic contact resistance $R_C = 10 \Omega$ was obtained by the transmission line method (TLM). Finally, a Ni/Au metal stack was deposited to form the gate electrode. The source-drain spacing (L_{SD}) is $20 \mu\text{m}$, and the gate width (W_G) is $100 \mu\text{m}$. The Schottky gate was symmetrically placed in the middle between the source and drain ohmic contacts. As shown in Fig. 1(b), the gate lengths (L_G) of Sample 1, 2, and 3 were $4 \mu\text{m}$, $10 \mu\text{m}$ and $16 \mu\text{m}$, respectively.

Measurements. Current-voltage (I - V) measurements and capacitance-voltage (C - V) measurements were performed by using an Agilent B1500A and Agilent B1520A Semiconductor Parameter Analyzers, respectively.

References

- Latorre-Rey, A. D., Sabatti, F. F. M., Albrecht, J. D. & Saraniti, M. Hot electron generation under large-signal radio frequency operation of GaN high-electron-mobility transistors. *Appl. Phys. Lett.* **111**, 013506, <https://doi.org/10.1063/1.4991665> (2017).
- Ma, J. & Matioli, E. Slanted tri-gates for high-voltage GaN power devices. *IEEE Electron Device Lett.* **38**, 1305–1308, <https://doi.org/10.1109/LED.2017.2731799> (2017).
- Tang, G. *et al.* Digital integrated circuits on an E-mode GaN power HEMT platform. *IEEE Electron Device Lett.* **38**, 1282–1285, <https://doi.org/10.1109/LED.2017.2725908> (2017).

4. Blaho, M. *et al.* Annealing, temperature, and bias-induced threshold voltage instabilities in integrated E/D-mode InAlN/GaN MOS HEMTs. *Appl. Phys. Lett.* **111**, 033506, <https://doi.org/10.1063/1.4995235> (2017).
5. Zhang, K. *et al.* High-Linearity AlGaIn/GaN FinFETs for Microwave Power Applications. *IEEE Electron Device Lett.* **38**, 615–618, <https://doi.org/10.1109/LED.2017.2687440> (2017).
6. Chiu, H. *et al.* RF Performance of *In Situ* SiNx Gate Dielectric AlGaIn/GaN MISHEMT on 6-in Silicon-on-Insulator Substrate. *IEEE Trans. Electron Devices.* **64**, 4065–4070, <https://doi.org/10.1109/TED.2017.2743229> (2017).
7. Sun, S. *et al.* AlGaIn/GaN metal-insulator-semiconductor high electron mobility transistors with reduced leakage current and enhanced breakdown voltage using aluminum ion implantation. *Appl. Phys. Lett.* **108**, 013507, <https://doi.org/10.1063/1.4939508> (2016).
8. Brown, D. F. *et al.* Self-Aligned AlGaIn/GaN FinFETs. *IEEE Electron Device Lett.* **38**, 1445–1448, <https://doi.org/10.1109/LED.2017.2747843> (2017).
9. Mi, M. *et al.* Millimeter-Wave Power AlGaIn/GaN HEMT Using Surface Plasma Treatment of Access Region. *IEEE Trans. Electron Devices.* **64**, 4875–4881, <https://doi.org/10.1109/TED.2017.2761766> (2017).
10. Ostermaier, C. *et al.* Dynamics of carrier transport via AlGaIn barrier in AlGaIn/GaN MIS-HEMTs. *Appl. Phys. Lett.* **110**, 173502, <https://doi.org/10.1063/1.4982231> (2017).
11. Yang, L. *et al.* Enhanced g_m and F_T With High Johnson's Figure-of-Merit in Thin Barrier AlGaIn/GaN HEMTs by TiN-Based Source Contact Edge. *IEEE Electron Device Lett.* **38**, 1563–1566, <https://doi.org/10.1109/LED.2017.2757523> (2017).
12. Suria, A. J. *et al.* Thickness engineering of atomic layer deposited Al₂O₃ films to suppress interfacial reaction and diffusion of Ni/Au gate metal in AlGaIn/GaN HEMTs up to 600 °C in air. *Appl. Phys. Lett.* **110**, 253505, <https://doi.org/10.1063/1.4986910> (2017).
13. Zhang, Y. *et al.* High-Temperature-Recessed Millimeter-Wave AlGaIn/GaN HEMTs With 42.8% Power-Added-Efficiency at 35 GHz. *IEEE Electron Device Lett.* **39**, 727–730, <https://doi.org/10.1109/LED.2018.2822259> (2018).
14. Mi, M. *et al.* 90 nm gate length enhancement-mode AlGaIn/GaN HEMTs with plasma oxidation technology for high-frequency application. *Appl. Phys. Lett.* **111**, 173502, <https://doi.org/10.1063/1.5008731> (2017).
15. Ambacher, O. *et al.* Two dimensional electron gases induced by spontaneous and piezoelectric polarization in undoped and doped AlGaIn/GaN heterostructures. *J. Appl. Phys.* **87**, 334, <https://doi.org/10.1063/1.371866> (2000).
16. Shinohara, K. *et al.* Scaling of GaN HEMTs and Schottky Diodes for Submillimeter-Wave MMIC Applications. *IEEE Trans. Electron Devices.* **60**, 2982–2996, <https://doi.org/10.1109/TED.2013.2268160> (2013).
17. Feng, Y. *et al.* Anisotropic strain relaxation and high quality AlGaIn/GaN heterostructures on Si (110) substrates. *Appl. Phys. Lett.* **110**, 192104, <https://doi.org/10.1063/1.4983386> (2017).
18. Chen, J. *et al.* Room-temperature mobility above 2200 cm²/V·s of two-dimensional electron gas in a sharp-interface AlGaIn/GaN heterostructure. *Appl. Phys. Lett.* **106**, 251601, <https://doi.org/10.1063/1.4922877> (2015).
19. Manfra, M. J. *et al.* Electron mobility exceeding 160000 cm²/V·s in heterostructures grown by molecular-beam epitaxy. *Appl. Phys. Lett.* **85**, 5394, <https://doi.org/10.1063/1.1824176> (2004).
20. Hao, R. *et al.* Breakdown Enhancement and Current Collapse Suppression by High-Resistivity GaN Cap Layer in Normally-Off AlGaIn/GaN HEMTs. *IEEE Electron Device Lett.* **38**, 1567–1570, <https://doi.org/10.1109/LED.2017.2749678> (2017).
21. Jiang, Q. *et al.* 1.4-kV AlGaIn/GaN HEMTs on a GaN-on-SOI Platform. *IEEE Electron Device Lett.* **34**, 357–359, <https://doi.org/10.1109/LED.2012.2236637> (2013).
22. Selvaraj, S. L. *et al.* 1.4-kV Breakdown Voltage for AlGaIn/GaN High-Electron-Mobility Transistors on Silicon Substrate. *IEEE Electron Device Lett.* **33**, 1357–1377, <https://doi.org/10.1109/LED.2012.2207367> (2012).
23. Bouzid-Driad, S. *et al.* AlGaIn/GaN HEMTs on Silicon Substrate With 206-GHz F_{MAX} . *IEEE Electron Device Lett.* **34**, 36–38, <https://doi.org/10.1109/LED.2012.2224313> (2013).
24. Liu, X. *et al.* AlGaIn/GaN Metal-Oxide-Semiconductor High-Electron-Mobility Transistor with Polarized P(VDF-TrFE) Ferroelectric Polymer Gating. *Sci. Rep.* **5**, 14092, <https://doi.org/10.1038/srep14092> (2015).
25. Pearton, S. J. & Ren, F. GaN Electronics. *Adv. Mater.* **12**, 1571, 10.1002/1521-4095(200011)12:21<1571::AID-ADMA1571>3.0.CO;2-T (2000).
26. Zhao, J. *et al.* Electron mobility related to scattering caused by the strain variation of AlGaIn barrier layer in strained AlGaIn/GaN heterostructures. *Appl. Phys. Lett.* **91**, 173507, <https://doi.org/10.1063/1.2798500> (2007).
27. Lv, Y. *et al.* Polarization Coulomb field scattering in AlGaIn/AlN/GaN heterostructure field-effect transistors. *Appl. Phys. Lett.* **98**, 123512, <https://doi.org/10.1063/1.3569138> (2011).
28. Luan, C. *et al.* Influence of the side-Ohmic contact processing on the polarization Coulomb field scattering in AlGaIn/AlN/GaN heterostructure field-effect transistors. *Appl. Phys. Lett.* **101**, 113501, <https://doi.org/10.1063/1.4752232> (2012).
29. Luan, C. *et al.* Polarization Coulomb field scattering in In_{0.18}Al_{0.82}N/AlN/GaN heterostructure field-effect transistors. *J. Appl. Phys.* **112**, 054513, <https://doi.org/10.1063/1.4752254> (2012).
30. Lv, Y. *et al.* Influence of the ratio of gate length to drain-to-source distance on the electron mobility in AlGaIn/AlN/GaN heterostructure field-effect transistors. *Nanoscale Res. Lett.* **7**, 434, <https://doi.org/10.1186/1556-276X-7-434> (2012).
31. Luan, C. *et al.* Theoretical model of the polarization Coulomb field scattering in strained AlGaIn/AlN/GaN heterostructure field-effect transistors. *J. Appl. Phys.* **116**, 044507, <https://doi.org/10.1063/1.4891258> (2014).
32. Luan, C. *et al.* Influence of polarization coulomb field scattering on the subthreshold swing in depletion-mode AlGaIn/AlN/GaN heterostructure field-effect transistors. *Physica E.* **62**, 76–79, <https://doi.org/10.1016/j.physe.2014.04.027> (2014).
33. Zhao, J. *et al.* Effects of rapid thermal annealing on the electrical properties of the AlGaIn/AlN/GaN heterostructure field-effect transistors with Ti/Al/Ni/Au gate electrodes. *Appl. Phys. Lett.* **105**, 083501, <https://doi.org/10.1063/1.4894093> (2014).
34. Zhao, J. *et al.* A study of the impact of gate metals on the performance of AlGaIn/AlN/GaN heterostructure field-effect transistors. *Appl. Phys. Lett.* **107**, 113502, <https://doi.org/10.1063/1.4931122> (2015).
35. Yang, M. *et al.* Study of source access resistance at direct current quiescent points for AlGaIn/GaN heterostructure field-effect transistors. *J. Appl. Phys.* **119**, 224501, <https://doi.org/10.1063/1.4953645> (2016).
36. Yang, M. *et al.* Study of gate width influence on extrinsic transconductance in AlGaIn/GaN heterostructure field-effect transistors with polarization Coulomb field scattering. *IEEE Trans. Electron Devices.* **63**, 3908–3913, <https://doi.org/10.1109/TED.2016.2597156> (2016).
37. Yang, M. *et al.* Effect of polarization Coulomb field scattering on parasitic source access resistance and extrinsic transconductance in AlGaIn/GaN heterostructure FETs. *IEEE Trans. Electron Devices.* **63**, 1471–1477, <https://doi.org/10.1109/TED.2016.2532919> (2016).
38. Cui, P. *et al.* Influence of different gate biases and gate lengths on parasitic source access resistance in AlGaIn/GaN heterostructure FETs. *IEEE Trans. Electron Devices.* **64**, 1038–1044, <https://doi.org/10.1109/TED.2017.2654262> (2017).
39. Cui, P. *et al.* Effect of polarization Coulomb field scattering on device linearity in AlGaIn/GaN heterostructure field-effect transistors. *J. Appl. Phys.* **122**, 124508, <https://doi.org/10.1063/1.5005518> (2017).
40. Cui, P. *et al.* Improved Linearity with Polarization Coulomb Field Scattering in AlGaIn/GaN Heterostructure Field-Effect Transistors. *Sci. Rep.* **8**, 983, <https://doi.org/10.1038/s41598-018-19510-y> (2018).
41. Anwar, A. F. M., Webster, R. T. & Smith, K. V. Bias induced strain in AlGaIn/GaN heterojunction field effect transistors and its implications. *Appl. Phys. Lett.* **88**, 203510, <https://doi.org/10.1063/1.2203739> (2006).
42. Fang, T. *et al.* Effect of Optical Phonon Scattering on the Performance of GaN Transistors. *IEEE Electron Device Lett.* **33**, 709–711, <https://doi.org/10.1109/LED.2012.2187169> (2012).

43. Li, T. *et al.* Monte Carlo evaluations of degeneracy and interface roughness effects on electron transport in AlGa_xN–Ga_{1-x}N heterostructures. *J. Appl. Phys.* **88**, 829, <https://doi.org/10.1063/1.373744> (2000).
44. Jena, D., Gossard, A. C. & Mishra, U. K. Dislocation scattering in a two-dimensional electron gas. *Appl. Phys. Lett.* **76**, 1707, <https://doi.org/10.1063/1.126143> (2000).
45. Xu, X. *et al.* Dislocation scattering in Al_xGa_{1-x}N/GaN heterostructures. *Appl. Phys. Lett.* **93**, 182111, <https://doi.org/10.1063/1.126143> (2008).
46. Ridley, B. K., Foutz, B. E. & Eastman, L. F. Mobility of electrons in bulk GaN and Al_xGa_{1-x}N/GaN heterostructures. *Phys. Rev. B.* **61**, 16862, <https://doi.org/10.1103/PhysRevB.61.16862> (2000).
47. Antoszewski, J. *et al.* Scattering mechanisms limiting two-dimensional electron gas mobility in Al_{0.25}Ga_{0.75}N/GaN modulation-doped field-effect transistors. *J. Appl. Phys.* **87**, 3900, <https://doi.org/10.1063/1.372432> (2000).
48. Hsu, L. & Walukiewicz, W. Electron mobility in Al_xGa_{1-x}N/GaN heterostructures. *Phys. Rev. B.* **56**, 1520, <https://doi.org/10.1103/PhysRevB.56.1520> (1997).
49. Polyakov, V. M. *et al.* Intrinsically limited mobility of the two-dimensional electron gas in gated AlGa_xN/GaN and AlGa_xN/AlN/GaN heterostructures. *J. Appl. Phys.* **106**, 023715, <https://doi.org/10.1063/1.3174441> (2009).
50. Gurusinge, M. N., Davidsson, S. K. & Andersson, T. G. Two-dimensional electron mobility limitation mechanisms in Al_xGa_{1-x}N/GaN heterostructures. *Phys. Rev. B.* **72**, 045316, <https://doi.org/10.1103/PhysRevB.72.045316> (2005).

Acknowledgements

This work was supported in part by the National Natural Science Foundation of China under Grant 11574182, Grant 11174182, Grant 61674130, Grant 11471194, Grant 11571115, and Grant 61504127, and in part by the Developing Foundation of CAEP under Grant 2014A05011.

Author Contributions

P.C. and Z.L. contributed to the research design, experiment measurements, data analysis, and manuscript preparation. J.M. and Y.L. fabricated the device. H.L. and A.C. carried out the mathematical calculation. C.F., C.L., Y.Z. and G.D. provided scientific advice. All authors reviewed this manuscript.

Additional Information

Competing Interests: The authors declare no competing interests.

Publisher's note: Springer Nature remains neutral with regard to jurisdictional claims in published maps and institutional affiliations.



Open Access This article is licensed under a Creative Commons Attribution 4.0 International License, which permits use, sharing, adaptation, distribution and reproduction in any medium or format, as long as you give appropriate credit to the original author(s) and the source, provide a link to the Creative Commons license, and indicate if changes were made. The images or other third party material in this article are included in the article's Creative Commons license, unless indicated otherwise in a credit line to the material. If material is not included in the article's Creative Commons license and your intended use is not permitted by statutory regulation or exceeds the permitted use, you will need to obtain permission directly from the copyright holder. To view a copy of this license, visit <http://creativecommons.org/licenses/by/4.0/>.

© The Author(s) 2018